A&A 483, 301–309 (2008)
DOI: 10.1051/0004-6361:20079128

Astronomy & Astrophysics

Radiative damping of standing acoustic waves in solar coronal loops

S. J. Bradshaw[1] and R. Erdélyi[2]

[1] Space and Atmospheric Physics, Blackett Laboratory, Imperial College London, Prince Consort Road, SW7 2BZ London, UK
e-mail: s.bradshaw@imperial.ac.uk
[2] Solar Physics and Space Plasma Research Centre (SP^{2}RC), Department of Applied Mathematics, University of Sheffield, Hicks Building, Hounsfield Road, S3 7RH Sheffield, UK

Received 23 November 2007 / Accepted 12 March 2008

ABSTRACT

Context. A detailed understanding of the physical processes that determine the damping timescales of magneto-acoustic waves is essential to interpret diagnostic results from the application of solar magneto-seismology.
Aims. The influence of the transition region and the importance of radiative emission, arising from equilibrium and non-equilibrium ionisation balances, for the damping timescale of the fundamental mode standing acoustic wave is investigated.
Methods. An extensive numerical study, in the framework of the field-aligned hydrodynamic approximation, is carried out of the damping of the fundamental mode standing wave in a solar coronal loop, for a wide range of loop lengths and apex temperatures.
Results. It was found that the radiative emission arising from a non-equilibrium ionisation balance will always act to reduce the damping timescale (in comparison to the equilibrium case) and may do so by up to ∼10%. The physics of the transition region is most crucial in determining the magnitude of the reduction of the damping timescale when a non-equilibrium ionisation balance is properly accounted for.
Conclusions. The methods of solar magneto-seismology, in particular the tools of coronal seismology, may be used to estimate loop lengths to a reasonable degree of accuracy, although estimates of the apex temperature are significantly less reliable, and one should use alternative (e.g. spectroscopic) diagnostics instead.

Key words. Sun: transition region – Sun: corona – Sun: UV radiation – atomic processes – hydrodynamics

1. Introduction

The magnetically complex solar corona supports a zoo of magnetohydrodynamic (MHD) waves. These MHD waves were theoretically predicted more than a full solar cycle ago, however, their existence in the solar corona was uniquely observed only after the launch of high-resolution space missions such as SOHO (SOlar and Heliospheric Observatory), TRACE (Transition Region And Coronal Explorer) and Hinode. The presence of a wide range of MHD waves allows several observationally relevant questions to be addressed. What is the relationship between the observed energy budget of the waves in comparison to the energy needed to maintain the observed unique temperature profile from the photosphere into the corona? What is their contribution to the acceleration of the solar wind? What is their role in carrying convective energy from sub-photospheric regions into the higher atmosphere? What is their role in the coupling of the various regions of the Sun? The observed properties of these waves (e.g. amplitudes, periods and damping timescales) can be used to deduce values for physical properties of the solar corona, as suggested by Roberts et al. (1984) in the context of coronal seismology. However, obtaining reliable diagnostic values requires a detailed understanding of the physical processes governing the behaviour of the wave modes used in the analysis. The method of coronal seismology was also applied to the lower solar atmosphere (Erdélyi 2006a,b), and the term solar atmospheric *magnetoseismology* was proposed (e.g. Banerjee et al. 2007). For recent reviews on magnetoseismology of the solar corona see Nakariakov & Verwichte (2005), Banerjee et al. (2007) and references therein. In the present work, acoustic (longitudinal slow-mode) waves will be of primary interest. In particular, the efficient damping of these waves by radiation processes in both equilibrium and non-equilibrium ionisation will be considered in detail.

Direct observations of spatially and temporally resolved magneto-acoustic waves (MAWs), *propagating* along coronal loops, were made available by the EIT instrument on board the SoHO satellite and have been discussed by Berghmans & Clette (1999). Propagating MAWs were later identified in TRACE observations by De Moortel et al. (2000, 2002a–c). Robbrecht et al. (2001) carried out a multi-instrument study of propagating MAWs using EIT and TRACE observations. The sources of these waves were identified by the authors as small-scale brightenings at one of the loop foot-points. Perhaps the most likely of the many possible explanations for the presence of these waves is the direct leakage of photospheric motions into the corona along tilted magnetic field lines (De Pontieu et al. 2003a,b, 2004, and 2005). However, none of these explanations have really addressed damping of the observed longitudinal MAWs and the potential importance of radiative emission from the plasma itself.

Conversely, oscillations that have been interpreted as *standing* MAWs have been observed in significantly hotter ($T >$ 6 MK) coronal loops by the SUMER instrument on board SoHO (Kliem et al. 2002; Wang et al. 2002, 2003a,b). Recently Taroyan et al. (2007b) have carried out forward modelling of these particular SUMER observations and described the observed oscillations, including their spectral signatures, from excitation to

damping. Although the spectral signatures were recovered with considerable accuracy, questions remained open regarding an efficient damping mechanism for the waves observed by SUMER, despite taking into account the complex radiative properties of the coronal plasma. The period of a standing MAW in a coronal loop can be expressed in terms of the sound speed and the loop length (Roberts et al. 1984), and standing and propagating MAWs can be differentiated from one another by examining the phase relationship between velocity and the intensity of optically thin emission lines. The phase difference is $1/4$ of a period for standing waves and zero for propagating waves. The SUMER data show clearly that the phase speeds derived from the observed periods and loop lengths are in good agreement with the sound speed, and that the intensity fluctuations lag the Doppler shifts by $1/4$ of a period.

The physical mechanism by which standing MAWs can be excited in coronal loops is not as clear as in the propagating case, due to a lack of observational clues. Numerical models have demonstrated the ready excitation of the second harmonic of a standing acoustic wave by impulsive coronal heating (Bradshaw & Mason 2003b; Bradshaw et al. 2004; Nakariakov et al. 2004; Tsiklauri et al. 2004), however, the waves observed by SUMER have periods corresponding to the fundamental mode. Taroyan et al. (2007a) has proposed a novel diagnostic tool how to identify the various harmonics through Doppler-shift studies of power spectra of oscillations in randomly (or otherwise) heated coronal loops. Through a model of spatio-temporal random energy releases concentrated near the footpoints of a coronal loop, proposed by Mendoza-Briceño et al. (2002, 2005), Mendoza-Briceño & Erdélyi (2006) studied the oscillatory response of coronal loops to random energy injections. Both standing and propagating longitudinal (i.e. acoustic) waves were found in the simulations. In particular, periodic features, such as wave packets, with periods of 150−220 s, 500−600 s and 800−1000 s were found. It was also shown that the periods increase with the loop length and decrease with the scale-length of the heating pulses.

Wang et al. (2003a, 2005) have also suggested that the fundamental mode standing acoustic wave could be excited by the injection of hot plasma at a loop transition region or chromospheric foot-point, driven by the reconnection of the existing magnetic field with emerging flux. Taroyan et al. (2005) provided numerical confirmation of this idea by showing that the fundamental mode standing acoustic wave can indeed be excited in a coronal loop by impulsive heating at a chromospheric foot-point, provided the duration of the pulse matches the period of the fundamental mode. More details on advances in forward modelling can be found in Taroyan et al. (2007b) using SUMER observations and in Taroyan & Bradshaw (2008) using Hinode EIS imaging and spectroscopic responses.

The *damping* of magneto-acoustic waves has also attracted a large amount of attention in recent years, since the damping timescale can reveal the dominant physical processes that control the energy balance of the coronal loops in which the waves are observed. The effect of thermal conduction on wave damping was investigated by Porter et al. (1994), Nakariakov et al. (2000), Ofman & Wang (2002), De Moortel et al. (2002c) and Mendoza-Briceño et al. (2004). The influence of compressive viscosity was studied by Porter et al. (1994), Nakariakov et al. (2000), Ofman et al. (2000) and Ofman & Wang (2002). Nakariakov et al. (2000) and Mendoza-Briceño et al. (2004) also included gravitational stratification, and McEwan et al. (2006) examined thermal stratification. In general, thermal conduction was found to be the dominant damping mechanism, although it was also found that the occurence of steeper velocity gradients under the influence of gravity could enhance the damping due to compressive viscosity, particularly in the hotter loops observed by SUMER (Mendoza-Briceño et al. 2004).

Radiation has been overlooked as a damping mechanism, largely because the coronal radiative energy losses are indeed small when compared with thermal conduction for the cases considered in previous works. However, when one considers the influence of a self-consistent transition region in the models, the roles of the various physical processes in the energy balance become less clear (Mendoza-Briceño et al. 2004). The transition region is considerably denser than the corona and also contains some of the most strongly emitting ions. Therefore, since the radiative energy loss is proportional to $n_{\rm e}^2$ (where $n_{\rm e}$ is the electron number density), one might expect a significant amount of the wave's energy to be lost from the transition region as it is transported to/from the corona during the lifetime of the wave (e.g. before its amplitude is damped by a factor of $1/e$). Furthermore, previous work has shown that the radiative emission curve can be strongly modified in the presence of a non-equilibrium ionisation balance (Spadaro et al. 1990; Hansteen 1993; Sarro et al. 1999; Teriaca et al. 1999; Bradshaw & Mason 2003a,b; Müller et al. 2003; Bradshaw et al. 2004; Müller et al. 2004). Hence, the purpose of the current work is to consider the influence of the transition region and the effect on the damping timescale of a standing acoustic wave due to the radiative energy losses that arise from equilibrium and non-equilibrium ionisation balances.

The paper is structured as follows: in Sect. 2 the numerical model is described; the results are presented and discussed in Sect. 3; and a summary of the work, the conclusions reached and ideas for future studies are given in Sect. 4.

2. Numerical model

The damping of a standing acoustic wave is studied by superimposing the velocity profile of the fundamental mode on an initially hydrostatic coronal loop in a one-dimensional geometry (Fig. 1, upper panel) and following the subsequent thermodynamic evolution of the plasma in time (t). The hydrostatic initial conditions describe a loop structured with a cool, dense chromosphere at each foot-point, self-consistent chromosphere-corona transition regions, and an overlying hot, tenuous corona. The spatial profile of the velocity wave is given by

$$v = v_0 \sin \frac{k\pi s}{L}, \tag{1}$$

where k is the mode number ($k = 1$ for the fundamental mode), s is the spatial coordinate along the magnetic field and L is the total length (foot-point to foot-point) of the loop (Fig. 1, lower panel). The hydrodynamic equations describing the thermodynamic evolution of the plasma are given by

$$\frac{\partial \rho}{\partial t} + \frac{\partial}{\partial s}(\rho v) = 0, \tag{2}$$

$$\frac{\partial}{\partial t}(\rho v) + \frac{\partial}{\partial s}\left(\rho v^2\right) = -\frac{\partial}{\partial s}(P_{\rm e} + P_{\rm i}) - \rho g_{\parallel}, \tag{3}$$

$$\frac{\partial E_{\rm e}}{\partial t} + \frac{\partial}{\partial s}\left[(E_{\rm e} + P_{\rm e})\, v\right] = -\frac{\partial F_{\rm ce}}{\partial s} + v\frac{\partial P_{\rm e}}{\partial s} + \frac{k_{\rm B} n}{\gamma - 1}\nu_{\rm ie}(T_{\rm i} - T_{\rm e}) + E_{\rm H} - E_{\rm R}, \tag{4}$$

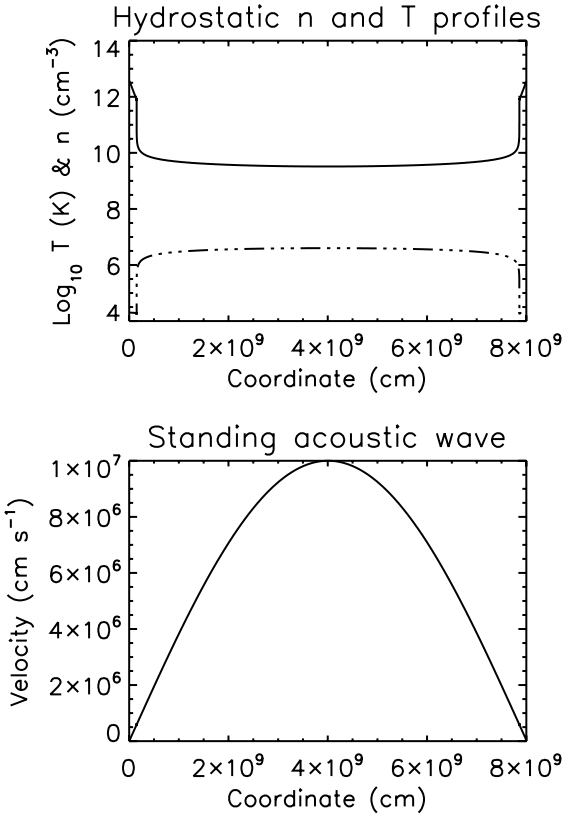

Fig. 1. *Upper panel*: number density (solid line) and temperature (triple-dash dot line) profiles for a hydrostatic loop of length $L = 8 \times 10^9$ cm and apex temperature $T_a = 4.0$ MK, with a uniform volumetric heating rate of $E_H = 4.9 \times 10^{-3}$ erg cm^{-3} s^{-1} required to maintain equilibrium. *Lower panel*: standing fundamental mode acoustic wave, with $v_0 = 10^7$ cm s^{-1}.

and

$$\frac{\partial E_i}{\partial t} + \frac{\partial}{\partial s}\left[(E_i + P_i)\, v\right] = -\frac{\partial F_{ci}}{\partial s} - v\frac{\partial P_e}{\partial s} + \frac{k_B n}{\gamma - 1}\nu_{ie}\,(T_e - T_i) + \rho v g_{\parallel}. \quad (5)$$

The plasma is considered to be composed of electrons and ions (mostly protons in the form of ionised hydrogen). In these equations a subscript e (i) denotes a property of the electron (ion) fluid. ρ, n and T are the mass density, number density and temperature, respectively. The closure conditions for Eqs. (2) to (5) give the energy densities,

$$E_e = \frac{P_e}{\gamma - 1},\ E_i = \frac{P_i}{\gamma - 1} + \frac{1}{2}\rho v^2 \quad (6)$$

(the electron kinetic energy is a factor m_e/m_i of the ion kinetic energy and is thus neglected) and pressures,

$$P_e = k_B n T_e,\ P_i = k_B n T_i. \quad (7)$$

The first term on the right-hand side of Eqs. (4) and (5) represents the thermally conducted flux carried by each particle species. The Spitzer coefficient for the electron thermal conduction is $\kappa_{0e} = 7.8 \times 10^{-7}$ erg cm^{-1} s^{-1} K$^{-7/2}$ and it is assumed that protons dominate the ion thermal conduction, giving $\kappa_{0i} = 3.2 \times 10^{-8}$ erg cm^{-1} s^{-1} K$^{-7/2}$. The second term on the right-hand side of Eqs. (4) and (5), the flux of the electron pressure, P_e, represents the work done by/on the particles due to the weak electric fields that arise from quasi-neutral conditions. The third term represents thermal equilibration between the particle species via collisions. The Coulomb collision frequency is given by

$$\nu_{ie} = \frac{16\sqrt{\pi}}{3}\frac{e^4}{m_e m_i}\left(\frac{2k_B T_e}{m_e}\right)^{-\frac{3}{2}} n\,(\ln\Lambda)\,, \quad (8)$$

where $\ln\Lambda$ is the Coulomb logarithm. Gravitational effects, where $g_\parallel$ is the component of gravity parallel to the magnetic field, have been included for the ion fluid and neglected for the electron fluid. E_H is the volumetric heating rate and its value in the current work is exactly that required to maintain the initial atmosphere in hydrostatic equilibrium. E_R is the volumetric rate of energy loss due to optically-thin radiative emission, which includes contributions from the emission lines of the most abundant elements found in the solar atmosphere and thermal bremsstrahlung. In the current work the radiative energy losses are calculated for both equilibrium and non-equilibrium ionisation balances in order to determine the relative importance of non-equilibrium radiative effects in the damping of standing acoustic waves. The ionisation balance (the relative abundance of the ions of a particular element) is given by

$$\frac{\partial Y_i}{\partial t} + \frac{\partial}{\partial s}\,(Y_i v) = n\,(I_{i-1}Y_{i-1} + R_i Y_{i+1} - I_i Y_i - R_{i-1}Y_i)\,, \quad (9)$$

where Y denotes the element (e.g. H, He, C, etc.) and i the ionisation stage. For example, $Y_{i=1}$ denotes neutral Y (or Y I in spectroscopic notation) and $Y_{i=2}$ denotes the first ionisation stage of Y (Y II), etc. Values of $Y_{i=1} = 0.25$ and $Y_{i=2} = 0.75$, for example, would show that 25% of element Y is present in the form of neutral Y and 75% is present in the form of singly-ionised Y. I and R are temperature dependent ionisation and recombination rates, respectively. The rates of Mazzotta et al. (1998) are used here. In equilibrium the time-dependent and velocity-dependent terms of Eq. (9) are neglected and the ionisation balance is a function of temperature only. Away from equilibrium, the ionisation balance exhibits a complicated dependence upon the local rate of ionisation/recombination and the transport of ions into/out of the emitting volume. The emissivity for a single element of atomic number Z is given by

$$\Lambda_Y = 0.83 \times Ab(Y) \times \sum_{i=1}^{Z+1} Y_i \times \epsilon_i, \quad (10)$$

where 0.83 is the proton:electron ratio, $Ab(Y)$ is the abundance of element Y relative to hydrogen and ϵ_i is the emissivity of ionisation stage i. The summation is over all ionisation stages (neutral to fully ionised). The ion emissivities used here are obtained from the Chianti database (Dere et al. 1997; Landi et al. 2006).

Finally, the volumetric rate of energy loss due to optically-thin radiative emission in Eq. (4) is given by

$$E_R = E_{RB} + n^2 \sum_Y \Lambda_Y, \quad (11)$$

where E_{RB} is thermal bremsstrahlung and the summation is over all of the elements with emission lines that make a significant contribution to the radiative energy loss. The fifteen most abundant elements in the set determined by Feldman (1992) are included in the radiation calculation (H, He, C, N, O, Ne, Na, Mg, Al, Si, S, Ar, Ca, Fe and Ni). Thus, as one can see, the non-equilibrium ionisation balance is coupled via Eqs. (9)–(11) to the hydrodynamic equation for the electron energy, Eq. (4).

Table 1. The uniform heating rates for the hydrostatic initial conditions.

	0.5 (MK)	1.0	2.0	4.0	8.0
2×10^9 cm	7.90×10^{-5} (erg cm^{-3} s^{-1})	1.10×10^{-3}	1.08×10^{-2}	...	...
4×10^9	1.50×10^{-5}	2.20×10^{-4}	2.30×10^{-3}	...	...
8×10^9	3.00×10^{-6}	5.50×10^{-5}	5.20×10^{-4}	4.90×10^{-3}	8.40×10^{-2}
16×10^9	5.00×10^{-7}	9.00×10^{-6}	1.10×10^{-4}	1.10×10^{-3}	1.60×10^{-2}

Table 1 shows the uniform heating rate (E_H) required to maintain equilibrium for each of the hydrostatic initial conditions, characterised by the loop length (L) and the apex temperature (T_a), that were used in the current work. The fundamental mode of a standing acoustic wave, with a maximum velocity amplitude $v_0 = 10^7$ cm s^{-1}, was superimposed on each of these initial conditions. The numerical code HYDRAD was then used to solve the coupled system of partial differential equations represented by Eqs. (2) to (7) and Eq. (9) to find the damping timescales of the fundamental mode for each set of initial conditions, both for equilibrium and non-equilibrium treatments of the ionisation balance and the associated radiative energy losses. Thus, a total of 32 numerical experiments were carried out. For details of the HYDRAD code and recent published results see: Bradshaw & Mason (2003b); Bradshaw et al. (2004); Bradshaw & Cargill (2006); Taroyan et al. (2007a); Taroyan et al. (2007b); and Taroyan & Bradshaw (2008).

The missing values in Table 1 indicate the region of the parameter space in which it was not feasible to carry out the numerical experiments due to computational constraints; these arose due to the small time steps associated with the electron thermal conduction term of Eq. (4) that were required to maintain numerical stability in short, hot loops. The numerical experiments for which the ionisation balance was treated in equilibrium in this region of the parameter space could be carried out fairly quickly, however, the run-times required by the experiments using the non-equilibrium treatment (a vastly more demanding problem) were considered impractical. In an effort to reduce the computational time for the $T_a = 4.0$ MK and $T_a = 8.0$ MK experiments, only the most abundant elements (H, He, C, O and Fe) were included in the non-equilibrium ionisation balance and radiative energy loss calculations. The remaining ten elements were treated in equilibrium. All fifteen elements were included in the non-equilibrium ionisation balance and radiative energy loss calculations for the $T_a < 4.0$ MK experiments.

Since the influence of the transition region on the damping timescales is of considerable interest in the current work it is necessary to ensure that adequate resolution is achieved. The vast range of spatial scales that exist in the solar atmosphere can make this a significant difficulty for numerical work. To solve this problem HYDRAD employs an adaptive grid, which has proven extremely effective at resolving the smallest scale features and tracking them as they propagate. In the current work the smallest grid cell is 10^4 cm (100 m).

3. Discussion of results

Figure 2 shows the profile of the absolute, normalised average velocity, $|\bar{v}/\bar{v_0}|$, during the decay of a fundamental mode standing wave. The plotted example is for $T_a = 0.5$ MK, $2 \times 10^9 \leq L \leq 16 \times 10^9$ cm and an equilibrium ionisation balance. The average velocity is defined by

$$\bar{v} = \frac{1}{L} \int_0^L v \mathrm{d}s \qquad (12)$$

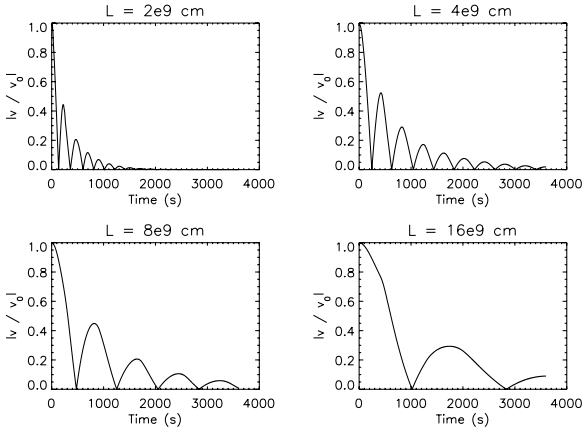

Fig. 2. The absolute, normalised average velocity, $|\bar{v}/\bar{v_0}|$, during the decay phase of the fundamental mode standing wave, for $T_a = 0.5$ MK, $2 \times 10^9 \leq L \leq 16 \times 10^9$ cm and an equilibrium ionisation balance.

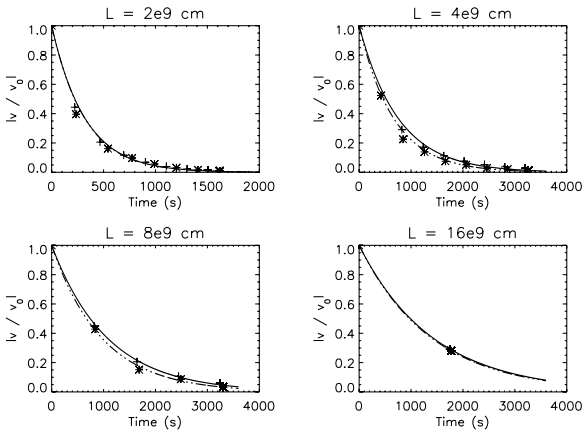

Fig. 3. Exponentially decaying curve fits to the peaks in $|\bar{v}/\bar{v_0}|$, along loops with $2 \times 10^9 \leq L \leq 16 \times 10^9$ cm, during the decay phase of the fundamental mode standing wave. The curve fits correspond to the mode decay for an equilibrium (+ symbol, solid line) and a non-equilibrium (* symbol, triple-dash dot line) ionisation balance. The apex temperature, T_a, of the initial hydrostatic equilibrium is 0.5 MK.

and $\bar{v_0}$ is the average velocity at $t = 0$ s. $\bar{v_0} \approx 6.4 \times 10^6$ cm s^{-1} for the velocity profile given in the lower panel of Fig. 1. Equation (12) was considered to provide a more suitable measure of the decay of the wave than choosing, for example, to plot the velocity at the apex of the loop as a function of time, because it characterises the decay of the wave along the entire length of the loop.

Figures 3 to 7 show the locations of the peaks in $|\bar{v}/\bar{v_0}|$ as the standing mode decays during each of the numerical experiments carried out in the present study. For example, the locations of the peaks in Fig. 2 are marked by the + symbols in the corresponding

Table 2. Damping timescales of the fundamental mode standing wave for an equilibrium ionisation balance. The associated percentage errors are quoted in brackets.

	0.5 (MK)	1.0	2.0	4.0	8.0
2×10^9 cm	321(8%) s	169(16%)	158(15%)	...	...
4×10^9	753(11%)	592(6%)	441(4%)	...	...
8×10^9	1071(4%)	1053(4%)	926(4%)	847(12%)	570(10%)
16×10^9	1424(0%)	1616(1%)	1593(2%)	1438(14%)	1161(10%)

Table 3. Damping timescales of the fundamental mode standing wave for a non-equilibrium ionisation balance. The associated percentage errors are quoted in brackets.

	0.5 (MK)	1.0	2.0	4.0	8.0
2×10^9 cm	319(10%) s	153(18%)	147(12%)	...	...
4×10^9	665(8%)	540(5%)	423(5%)	...	...
8×10^9	966(5%)	968(4%)	866(3%)	792(13%)	556(9%)
16×10^9	1395(0%)	1499(3%)	1534(1%)	1414(13%)	1116(12%)

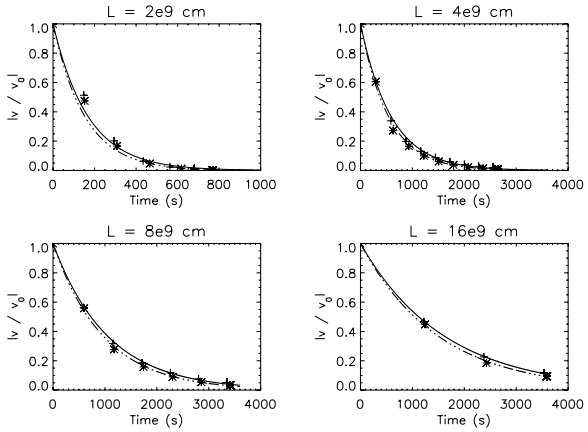

Fig. 4. As Fig. 3 for $T_a = 1.0$ MK.

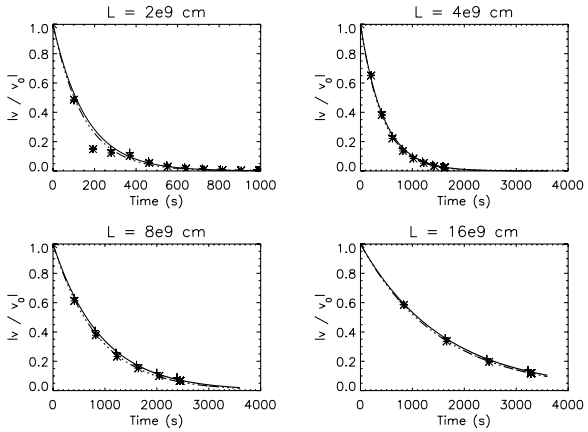

Fig. 5. As Fig. 3 for $T_a = 2.0$ MK.

plots in Fig. 3. Figures 3 to 7 also show exponential curve fits to the locations of the peaks. The curve fits have the form

$$\left|\frac{\bar{v}}{\bar{v}_0}\right| = \exp\left(-\frac{t}{\tau}\right), \tag{13}$$

from which the damping timescales, τ, can be estimated. These are given in Tables 2 and 3, which show the damping timescales of the fundamental mode standing wave in a loop of length (L) and apex temperature (T_a) for equilibrium and non-equilibrium ionisation balances. The nature of the damping is not exactly

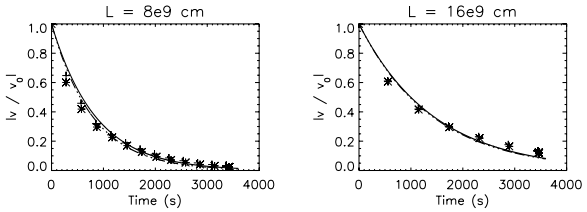

Fig. 6. As Fig. 3 for $8 \times 10^9 \leq L \leq 16 \times 10^9$ cm and $T_a = 4.0$ MK.

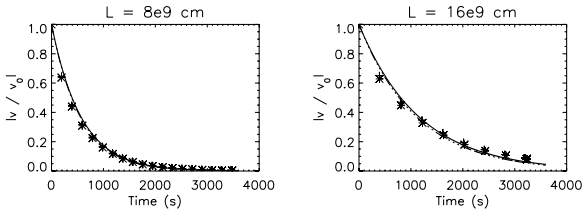

Fig. 7. As Fig. 3 for $8 \times 10^9 \leq L \leq 16 \times 10^9$ cm and $T_a = 8.0$ MK.

exponential; the wave decays initially somewhat more rapidly than at later times and so the given damping timescales may be regarded as averages over the decay phase. The percentage errors associated with the damping timescales give the root-mean-square deviation of the quoted value from the damping timescale at any particular time during the decay phase. Thus, the errors are correlated in the sense that whenever the average damping timescale is an underestimate (overestimate) during a numerical experiment for an equilibrium ionisation balances then it is an underestimate (overestimate) in the corresponding experiment for a non-equilibrium ionisation balance.

Though such a simple description as an exponential decay would, of course, not be expected for such a complex process in which several physical mechanisms operate, it is an adequate characterisation to provide an intuitive indication of the relative magnitude of the radiative contribution to the damping timescale, for equilibrium and non-equilibrium ionisation balances.

As expected, the shorter or hotter the loop the smaller the damping timescale of the fundamental mode standing wave and it is also clear that radiation due to a non-equilibrium ionisation balance leads to consistently smaller estimates for the damping timescale in comparison with the corresponding equilibrium case. The percentage differences between the damping timescales for the equilibrium and non-equilibrium cases in

Table 4. The percentage difference between the damping timescales in Tables 2 and 3.

	0.5 (MK)	1.0	2.0	4.0	8.0
2×10^9 cm	0.6%	9.5%	7.0%	...	...
4×10^9	11.7%	8.8%	4.1%	...	...
8×10^9	9.8%	8.0%	6.5%	6.5%	2.5%
16×10^9	2.0%	7.2%	3.7%	1.7%	3.9%

Tables 2 and 3 are given in Table 4, which shows that the damping timescale can be reduced by up to ∼10%. There is no clear tendency to indicate exactly how significant the effect of a non-equilibrium ionisation balance on the damping timescale will be for a loop of given length, although it is generally the case that the magnitude of the effect is reduced for hotter loops. The densities in high temperature, near-hydrostatic loops are greater than in cooler, near-hydrostatic loops, thus collisional timescales are reduced and the ionisation balance will be closer to equilibrium.

One might be tempted to generalise and suggest that the ionisation balance is likely to be close to equilibrium in all loops with densities above a certain threshold. However, to do so would be to miss several extremely important and more subtle aspects of the behaviour of the ionisation balance. In the present work the ionisation balance is driven away from equilibrium by the interaction between the bulk flow and the temperature gradient, and it is driven towards equilibrium by ionisation/recombination at a rate dependent upon the density. The ionisation balance will be driven further from equilibrium by stronger flows and steeper temperature gradients, and closer to equilibrium by higher densities. Understanding the interplay between these processes is crucially important to understanding the behaviour of the ionisation balance and determining its effect upon the damping timescale.

Figures 6 and 7 show that the damping timescales for the loops with $4.0 \leq T_a \leq 8.0$ MK are very similar for each corresponding equilibrium and non-equilibrium case, and so the ionisation balance must always remain close to equilibrium. The loops in these two figures are hot and dense, but also relatively long ($8 \times 10^9 \leq L \leq 16 \times 10^9$ cm) and so the temperature gradient is comparatively shallow relative to the bulk flow velocity. A significantly stronger bulk flow would be required to transport ions across the temperature gradient before they could equilibrate with their surroundings, and drive the ionisation balance sufficiently far from equilibrium that it may have an effect upon the damping timescale. One might expect that the ionisation balance in loops with $4.0 \leq T_a \leq 8.0$ MK and $L < 8 \times 10^9$ cm would be driven further from equilibrium than in the cases with $L \geq 8 \times 10^9$ cm, due to the steeper temperature gradients that would be present in the hydrostatic initial conditions. However, a steeper temperature gradient implies an enhanced heat flux from the corona and in order to drive the necessary heat flux it follows that the radiative energy loss from the transition region must increase. Since $R \propto n^2$ the density must also increase and the ionisation balance may then be driven towards equilibrium. The density may also be increased due to chromospheric evaporation driven by the heat flux. It is worth bearing in mind that the non-equilibrium ionisation balance was calculated for a reduced set of elements in these cases in order to speed up the calculations and the effect of a non-equilibrium ionisation balance may consequently be somewhat underestimated. However, the chosen elements are the most abundant and radiate the most strongly, and the addition of elements to the non-equilibrium ionisation balance calculations is not expected to alter these results significantly.

Figures 3 to 5 show some evidence for the effect of the interplay between the processes described above on the ionisation balance and the effect on the damping timescale. Consider Fig. 3 in which the temperature gradient is relatively shallow for all L since $T_a = 0.5$ MK. The decay profiles for the equilibrium and non-equilibrium ionisation balances are almost identical for the $L = 2 \times 10^9$ cm case, despite the shift in the locations of the peaks (the + and * symbols are not temporally coincident). This suggests that the effect of the temporal offset of the peaks in the non-equilibrium case coupled with the slightly smaller amplitude of each peak compared with the corresponding peak in the equilibrium case cancel, resulting in the same damping timescale for each case. The decay profiles differ between the equilibrium and non-equilibrium cases for the loops with $L = 4 \times 10^9$ and $L = 8 \times 10^9$ cm, with the damping timescales reduced in the non-equilibrium cases. Due to the low densities in these cases, the collisional timescales are not small enough for the ionisation balance to equilibrate as ions are transported across the temperature gradient, even though it is relatively shallow. The decay curve is only fitted to two peaks for the loop with $L = 16 \times 10^9$ cm (at $t = 0$ and $t \approx 1760$ s), though it is evident that the second peaks are more or less temporally coincident with very similar values for the relative velocities. This suggests that although the densities are the lowest encountered in any of the numerical experiments, the temperature gradient is sufficiently shallow that there is time for the ionisation balance to be collisionally equilibrated as ions are transported by the bulk flow.

The decay profiles of the $T_a = 1.0$ MK loops in Fig. 4 all exhibit differences between the equilibrium and non-equilibrium cases, with the damping timescales reduced in the non-equilibrium cases. Despite the higher densities and smaller collisional equilibration timescales in these hotter loops, compared with the corresponding $T_a = 0.5$ MK loops in Fig. 3, the non-equilibrium nature of the ionisation balances suggests a significant sensitivity to the temperature gradients, which are steeper in Fig. 4 than in Fig. 3. The temperature gradients of the $T_a = 2.0$ MK loops in Fig. 5 are steeper than in the previous two figures, but their densities are also greater and collisional equilibration is better able to mitigate the sensitivity of the ionisation balance to the temperature gradient. The $T_a = 4.0$ and $T_a = 8.0$ MK loops in Figs. 6 and 7 continue this trend, as already discussed.

Overall, these results indicate the existence of regimes, dependent upon the densities and the strength of the bulk flow relative to the temperature gradient, within which the ionisation balance may have a significant effect in reducing the damping timescale of the fundamental mode standing wave. However, this may not be the full picture since one must also consider the atomic properties of the particular population of emitting ions. For example, as discussed, one might expect the ionisation balance to be closest to equilibrium in the hottest and most dense loops, but it is also true that the ionisation potentials for the correspondingly more highly charged population of ions are greater, which makes them more difficult to ionise as they are transported across a steep, positive temperature gradient and drives the ionisation balance away from equilibrium. Furthermore, highly charged ions generally radiate more weakly than lower charge states and a non-equilibrium population of ions, formed at a lower temperature than the local temperature of the plasma, would tend to radiate more strongly under these conditions, thus increasing the rate of energy loss from the loop and reducing the damping timescales accordingly. Therefore, when

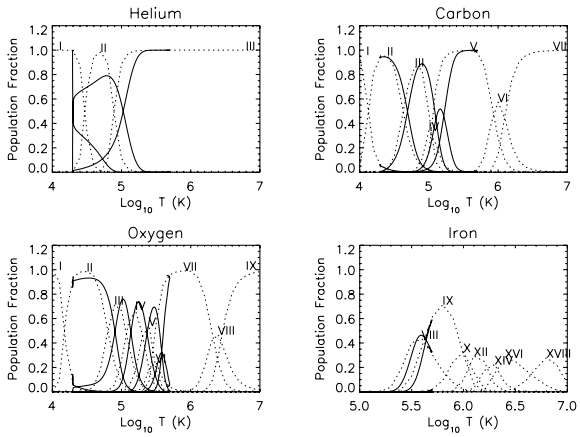

Fig. 8. The non-equilibrium ionisation balance (solid line) of He, C, O and Fe for the case $L = 8 \times 10^9$ cm and $T_a = 0.5$ MK at $t = \tau$ (966 s in Table 3). The equilibrium ionisaton balance (dotted line) is plotted for comparison.

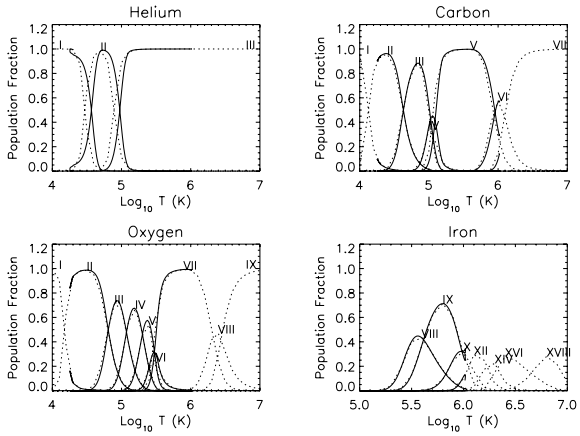

Fig. 9. As Fig. 8 for $L = 8 \times 10^9$ cm and $T_a = 1.0$ MK at $t = 968$ s.

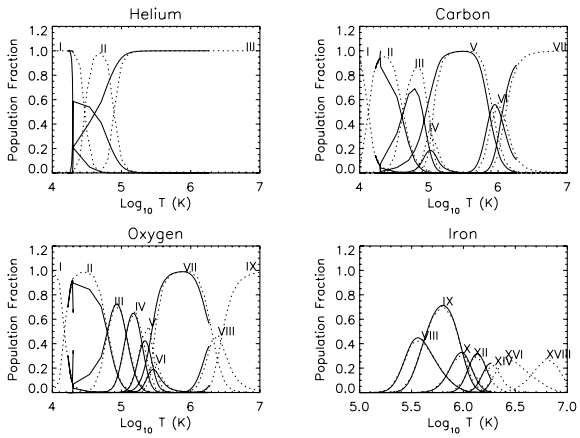

Fig. 10. As Fig. 8 for $L = 8 \times 10^9$ cm and $T_a = 2.0$ MK at $t = 866$ s.

one considers the effects of a non-equilibrium ionisation balance one must appreciate the interaction between the physical and dynamical properties of the plasma and the atomic properties of the ion population. This adds a substantial layer of complexity to the problem.

Figures 8 to 12 show the ionisation balances of the elements He, C, O and a selection of Fe ions (these are among the most strongly radiating elements in the solar atmosphere) in the

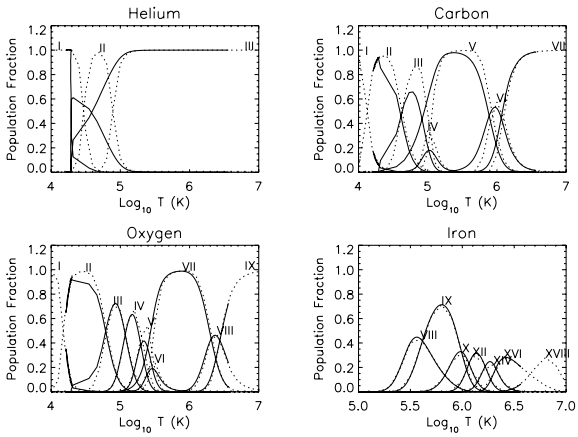

Fig. 11. As Fig. 8 for $L = 8 \times 10^9$ cm and $T_a = 4.0$ MK at $t = 792$ s.

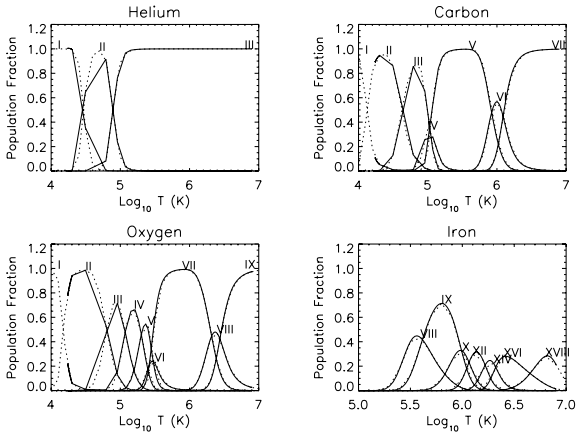

Fig. 12. As Fig. 8 for $L = 8 \times 10^9$ cm and $T_a = 8.0$ MK at $t = 556$ s.

left-hand leg of the loop ($s < L/2$) for the cases $L = 8 \times 10^9$ cm and $0.5 \leq T_a \leq 8.0$ MK. The non-equilibrium ionisation balance is taken at $t = \tau$, when the amplitude of the fundamental mode standing wave has decayed by a factor $1/e$, and plotted with the corresponding equilibrium ionisation balances for comparison. In Figs. 8 and 9 it is clear that the ionisation balances have essentially shifted to higher temperatures (via transport across the temperature gradient) and, as mentioned above, ions will generally radiate more strongly at temperatures that are higher than their equilibrium formation temperatures. Thus, shifting the ionisation balances to higher temperatures will result in a greater rate of energy loss from the loop and hence more efficient damping, as observed from the numerical experiments. Generally, the ionisation balances oscillate between higher and lower temperatures as the wave decays (the velocity amplitude changes sign and ions are transported in the opposite direction), as can be seen in Figs. 10 and 11 where the ionisation balance has shifted to lower temperatures. When the ions are transported to higher temperatures they encounter lower densities and so their non-equilibrium states persist. Conversely, when the ions are transported to lower temperatures they encounter higher densities and equilibrate more rapidly. The effect on the non-equilibrium ionisation balance is a larger population of lower charge states than would be found in equilibrium and, since lower charge states generally radiate more strongly than higher charge states, correspondingly greater radiative losses and reduced damping timescales in the non-equilibrium cases. The ionisation balances are very close to equilibrium in Fig. 12.

Table 5. Values of α calculated from the damping timescales in Tables 2 and 3.

T (MK)	Equilibrium	Non-equilibrium
0.5	0.7 (R^2 = 0.9282)	0.7 (R^2 = 0.9664)
1.0	1.06 (R^2 = 0.9361)	1.07 (R^2 = 0.9376)
2.0	1.11 (R^2 = 0.9804)	1.11 (R^2 = 0.9802)

Table 6. Values of β calculated from the damping timescales in Tables 2 and 3.

L (cm)	Equilibrium	Non-equilibrium
2×10^9	–0.51 (R^2 = 0.8205)	–0.56 (R^2 = 0.7886)
4×10^9	–0.39 (R^2 = 0.9966)	–0.33 (R^2 = 0.9979)
8×10^9	–0.21 (R^2 = 0.8317)	–0.19 (R^2 = 0.8145)
16×10^9	–0.08 (R^2 = 0.3940)	–0.07 (R^2 = 0.3239)

A common feature of the ionisation balances in all of Figs. 8 to 12 is that the populations of ions formed at lower (transition region) temperatures exhibit far stronger departures from equilibrium with the thermal properties of the plasma, despite the fact that the strongest flows are found at higher (coronal) temperatures (since the anti-node of the fundamental mode standing wave is located at the loop apex). This emphasises the sensitivity of the ionisation balance to the transition region temperature gradient and shows that it is the physics of the transition region that is responsible for the reduced damping timescales when non-equilibrium processes on the ionisation balance are properly accounted for. Therefore, as also shown by Bradshaw & Cargill (2005), the transition region can be very important in governing the dynamical behaviour of the entire loop. The populations of the more highly charged ions found at coronal temperatures remain closer to equilibrium due to the much shallower temperature gradients. Clearly, the non-equilibrium ionisation balances induced by the decay of the fundamental mode standing wave will affect the properties of the transition region emission lines that may be used for spectroscopic diagnostic purposes, but the results discussed here also show that diagnostics with coronal emission lines should be reliable for use in coronal seismology applications.

As an example, consider a set of observations of the decay of a fundamental mode standing wave in a coronal loop from which spectroscopically derived measurements of T_a (from line ratios) and v (from Doppler shifts) can be obtained. The damping timescale, τ, can be calculated from the Doppler shifts. These results can then be used to determine L, a traditionally difficult measurement to make due to projection and line-of-sight effects. The question to be addressed is what effect does the non-equilibrium ionisation balance that may be induced in the transition region have on the reliability of the measurement of L?

If it is assumed that the damping timescale varies as some power of the length or temperature of the loop, e.g. $\tau \propto L^{\alpha}$ or $\tau \propto T^{\beta}$, then the values of the power-law indices α and β can be estimated for constant length or temperature from the damping timescales in Tables 2 and 3.

Tables 5 and 6 show the values of α and β calculated using a least-squares fit, and the corresponding coefficient of determination (R^2), for constant values of T_a and L. Table 5 shows that the dependence of the damping timescale on L is approximately linear for both equilibrium and non-equilibrium ionisation balances. Table 6 shows that the damping timescale exhibits a gradually weakening dependence on T_a with increasing L. The power-law fits for $L = 16 \times 10^9$ cm are relatively poor due to the lack of peak locations in Figs. 3 to 7 from which to calculate the decay timescales. For example, in Fig. 3 there are only two peaks in the profile of $|\bar{v}|$ for $L = 16 \times 10^9$ cm; one at $t = 0$ and another at $t \approx 1760$ s. However, the general trend is indicative and shows that for the longest loops the damping timescale of the fundamental mode standing wave is only weakly dependent upon T_a.

The values of α for the equilibrium and non-equilibrium cases in Table 5 are essentially identical, with values of R^2 very close to 1.0. Therefore, given the values of T_a (as obtained from line ratios) to select an appropriate value of α and τ (as obtained from Doppler shifts), one may determine L and be confident that a non-equilibrium ionisation balance induced in the transition region should not have a significant effect on the result. Conversely, Table 6 shows that T_a could be obtained from measurements of L with considerably less accuracy for shorter loops and not at all for longer loops.

4. Summary, conclusions and future work

A detailed understanding of the physical processes that determine the damping timescales of MAWs is essential to the interpretation of diagnostic results obtained from the application of magneto-seismology. An extensive numerical study of the damping of the fundamental mode standing wave in a solar coronal loop, for a wide range of loop lengths and apex temperatures, has been carried out in order to assess the influence of the transition region and the importance of radiative energy losses, arising from equilibrium and non-equilibrium ionisation balances, on the damping timescale.

It has been found that the radiative emission arising from a non-equilibrium ionisation balance will always act to reduce the damping timescale (in comparison to the equilibrium case) and may do so by up to ~10%. Mendoza-Briceño et al. (2004) found a similar order of reduction in the damping timescale when they included gravitational stratification. A non-equilibrium ionisation balance acts to reduce the damping timescale due to a bias towards the existence of lower charge states, which gives rise to greater radiative energy losses because lower charge states tend to radiate more strongly than higher charge states.

The population of ions formed at transition region temperatures exhibit the strongest departures from equilibrium, which emphasises the sensitivity of the ionisation balance to the transition region temperature gradient and shows that the physics of the transition region is most crucial in determining the magnitude of the reduction of the damping timescale when a non-equilibrium ionisation balance is properly accounted for.

Overall, these results indicate the existence of regimes, dependent upon a coupling between the density, the strength of the bulk flow relative to the temperature gradient and the atomic properties of the emitting ions, within which the ionisation balance may have a significant (of order 10%) effect in reducing the damping timescale of the fundamental mode standing wave.

The ionisation balance induced in the transition region by the decay of the fundamental mode standing wave may also affect the properties of the emission lines used for spectroscopic diagnostics. However, due to the shallower temperature gradients, diagnostics with coronal emission lines should be reliable.

Finally, as an application of coronal seismology, it has been found that given a reliable determination of the apex temperature and the damping timescale using spectroscopic diagnostic methods, one may estimate the loop length to a reasonable degree of accuracy and be confident that a non-equilibrium ionisation balance in the transition region should not introduce any significant

ambiguity to the result. Conversely, it has been shown that one should not attempt to estimate the apex temperature from measurements of the loop length and the damping timescale.

There are a number of avenues along which the current work might profitably be extended. A regime of substantially stronger bulk flows would provide more strongly non-equilibrium ionisation balances and may affect the conclusion regarding the reliability of a determination of the loop length, L, from T_a and τ. However, in the lower temperature and lower density range of the parameter space, the chosen maximum bulk flow velocity of 10^7 cm s^{-1} has a relatively large Mach number, and so this effect has been accounted for to some extent. However, it would be interesting to study a regime of constant Mach number with varying L and T_a. At the higher densities implied by higher temperatures, one may expect the correspondingly greater rates of ionisation and recombination to drive the ionisation balance towards equilibrium, although, as discussed in the text, the atomic properties of the ions may also have an important effect.

One important extension of the present investigation would be the self-consistent generation of a fundamental mode standing wave (as in Taroyan et al. 2005) rather than imposing a fundamental mode velocity profile on a hydrostatic solution, and following its subsequent decay.

As shown by De Moortel & Bradshaw (2008), the physical properties of coronal perturbations can be very difficult to recover from observational data alone and one must look to forward-modeling in order to guide the interpretation of observational results. Therefore, an important extension of the present work would be the generation of synthetic observations, using forward-modeling techniques, in order to identify spectral signatures of the damping of fundamental mode standing waves and to assess their reliability in terms of recovering the underlying physics of this process.

Acknowledgements. S.B. is grateful to the STFC for their support through the award of a Post-Doctoral Fellowship. R.E. acknowledges M. Kéray for patient encouragement and is also grateful to the NSF, Hungary (OTKA, Ref. No. K67746) for the financial support received.

References

Banerjee, D., Erdélyi, R., Oliver, R., & O'Shea, E. 2007, Sol. Phys., 136
Berghmans, D., & Clette, F. 1999, Sol. Phys., 186, 207
Bradshaw, S. J., & Mason, H. E. 2003a, A&A, 401, 699
Bradshaw, S. J., & Mason, H. E. 2003b, A&A, 407, 1127
Bradshaw, S. J., & Cargill, P. J. 2005, A&A, 437, 311
Bradshaw, S. J., & Cargill, P. J. 2006, A&A, 458, 987
Bradshaw, S. J., Del Zanna, G., & Mason, H. E. 2004, A&A, 425, 287
De Moortel, I., & Bradshaw, S. J. 2008, Sol. Phys., submitted
De Moortel, I., Ireland, J., & Walsh, R. W. 2000, A&A, 355, L23
De Moortel, I., Hood, A. W., Ireland, J., & Walsh, R. W. 2002a, Sol. Phys., 209, 89
De Moortel, I., Ireland, J., Hood, A. W., & Walsh, R. W. 2002b, A&A, 387, L13
De Moortel, I., Ireland, J., Walsh, R. W., & Hood, A. W. 2002c, Sol. Phys., 209, 61
De Pontieu, B., Erdélyi, R., & de Wijn, A. G. 2003a, ApJ, 595, L63
De Pontieu, B., Tarbell, T., & Erdélyi, R. 2003b, ApJ, 590, 502
De Pontieu, B., Erdélyi, R., & James, S. P. 2004, Nature, 430, 536
De Pontieu, B., Erdélyi, R., & De Moortel, I. 2005, ApJ, 624, L61
Dere, K. P., Landi, E., Mason, H. E., Monsignori Fossi, B. C., & Young, P. R. 1997, A&AS, 125, 149
Erdélyi, R. 2006a, Royal Soc. London Philos. Trans. Ser. A, 364, 351
Erdélyi, R. 2006b, in ESA Special Publication, 624, Proceedings of SOHO 18/GONG 2006/HELAS I, Beyond the spherical Sun
Feldman, U. 1992, Phys. Scri., 46, 202
Hansteen, V. 1993, ApJ, 402, 741
Kliem, B., Dammasch, I. E., Curdt, W., & Wilhelm, K. 2002, ApJ, 568, L61
Landi, E., Del Zanna, G., Young, P. R., et al. 2006, ApJS, 162, 261
Mazzotta, P., Mazzitelli, G., Colafrancesco, S., & Vittorio, N. 1998, A&AS, 133, 403
McEwan, M. P., Donnelly, G. R., Díaz, A. J., & Roberts, B. 2006, A&A, 460, 893
Mendoza-Briceño, C. A., & Erdélyi, R. 2006, ApJ, 648, 722
Mendoza-Briceño, C. A., Erdélyi, R., & Di G. Sigalotti, L. 2002, ApJ, 579, L49
Mendoza-Briceño, C. A., Erdélyi, R., & Sigalotti, L. D. G. 2004, ApJ, 605, 493
Mendoza-Briceño, C. A., Sigalotti, L. D. G., & Erdélyi, R. 2005, ApJ, 624, 1080
Müller, D. A. N., Hansteen, V. H., & Peter, H. 2003, A&A, 411, 605
Müller, D. A. N., Peter, H., & Hansteen, V. H. 2004, A&A, 424, 289
Nakariakov, V. M., & Verwichte, E. 2005, Living Rev. Sol. Phys., 2, 3
Nakariakov, V. M., Verwichte, E., Berghmans, D., & Robbrecht, E. 2000, A&A, 362, 1151
Nakariakov, V. M., Tsiklauri, D., Kelly, A., Arber, T. D., & Aschwanden, M. J. 2004, A&A, 414, L25
Ofman, L., & Wang, T. 2002, ApJ, 580, L85
Ofman, L., Nakariakov, V. M., & Sehgal, N. 2000, ApJ, 533, 1071
Porter, L. J., Klimchuk, J. A., & Sturrock, P. A. 1994, ApJ, 435, 502
Robbrecht, E., Verwichte, E., Berghmans, D., et al. 2001, A&A, 370, 591
Roberts, B., Edwin, P. M., & Benz, A. O. 1984, ApJ, 279, 857
Sarro, L. M., Erdélyi, R., Doyle, J. G., & Pérez, M. E. 1999, A&A, 351, 721
Spadaro, D., Zappala, R. A., Antiochos, S. K., Lanzafame, G., & Noci, G. 1990, ApJ, 362, 370
Taroyan, Y., & Bradshaw, S. J. 2008, A&A, submitted
Taroyan, Y., Erdélyi, R., Doyle, J. G., & Bradshaw, S. J. 2005, A&A, 438, 713
Taroyan, Y., Erdélyi, R., Doyle, J. G., & Bradshaw, S. J. 2007a, A&A, 462, 331
Taroyan, Y., Erdélyi, R., Wang, T. J., & Bradshaw, S. J. 2007b, ApJ, 659, L173
Teriaca, L., Doyle, J. G., Erdélyi, R., & Sarro, L. M. 1999, A&A, 352, L99
Tsiklauri, D., Nakariakov, V. M., Arber, T. D., & Aschwanden, M. J. 2004, A&A, 422, 351
Wang, T., Solanki, S. K., Curdt, W., Innes, D. E., & Dammasch, I. E. 2002, ApJ, 574, L101
Wang, T. J., Solanki, S. K., Curdt, W., et al. 2003a, A&A, 406, 1105
Wang, T. J., Solanki, S. K., Innes, D. E., Curdt, W., & Marsch, E. 2003b, A&A, 402, L17
Wang, T. J., Solanki, S. K., Innes, D. E., & Curdt, W. 2005, A&A, 435, 753